Photodiagnosis and Photodynamic Therapy 26 (2019) 436–441

Contents lists available at ScienceDirect

Photodiagnosis and Photodynamic Therapy

journal homepage: www.elsevier.com/locate/pdpdt

Photoacoustic diagnosis of pharmacokinetics and vascular shutdown effects in photodynamic treatment with indocyanine green-lactosome for a subcutaneous tumor in mice

Yasuyuki Tsunoi[a], Koji Araki[b], Eiichi Ozeki[c], Isao Hara[c], Akihiro Shiotani[b], Mitsuhiro Terakawa[d,e], Shunichi Sato[a,*]

[a] Division of Bioinformation and Therapeutic Systems, National Defense Medical College Research Institute, 3-2 Namiki, Tokorozawa, Saitama 359-8513, Japan
[b] Department of Otolaryngology-Head and Neck Surgery, National Defense Medical College, 3-2 Namiki, Tokorozawa, Saitama 359-8513, Japan
[c] Technology Research Laboratory, Shimadzu Corporation, 3-9-4 Hikaridai, Seika-cho, Soraku-gun, Kyoto 619-0237, Japan
[d] Department of Electronics and Electrical Engineering, Keio University, 3-14-1 Hiyoshi, Kohoku-ku, Yokohama, Kanagawa 223-8522, Japan
[e] School of Integrated Design Engineering, Keio University, 3-14-1 Hiyoshi, Kohoku-ku, Yokohama, Kanagawa 223-8522, Japan

ARTICLE INFO

Keywords:
Photodynamic therapy
Photoacoustic imaging
Photosensitizer dosimetry
Vascular shutdown
Biodegradable nanomicelles
Indocyanine green-lactosome

ABSTRACT

Indocyanine green lactosome (ICG-lactosome) is an attractive new-generation agent for photodynamic therapy (PDT) that is characterized by a near-infrared excitation wavelength and high stability in the bloodstream. Fluorescence imaging has been used to examine its pharmacokinetics *in vivo*, but no depth-resolved information can be obtained with this method. In this study, we applied photoacoustic (PA) imaging to visualize the depth distribution of ICG-lactosome in a mouse subcutaneous tumor model. With this method, the depth distribution of blood vessels can also be visualized, enabling detection of vascular shutdown effects due to PDT. We performed PA imaging of both the distributions of ICG-lactosome and blood vessels in a tumor before and after PDT, and we found that PA signals originating from ICG-lactosome were greatly increased at 18 h after drug injection but rapidly decreased after PDT. These results indicate efficient accumulation of ICG-lactosome and rapid photobleaching due to the PDT reaction in the tumor, respectively. After PDT, PA amplitudes of hemoglobin were significantly decreased, being attributable to vascular shutdown effects. These results show the usefulness of PA imaging for monitoring not only photosensitizer accumulation and bleaching but also vascular responses in PDT with ICG-lactosome. This method can be applied to the diagnosis of many types of PDT processes.

1. Introduction

Photosensitizer (PS)-loaded nanocarriers (NCs), such as those using liposomes and micelles, have recently received much attention as new-generation agents for photodynamic therapy (PDT) due to their potentially efficient accumulation in tumors through an enhanced permeation and retention (EPR) effect [1], high stability in the bloodstream and capability of adding certain functions on the carriers [2–4]. As a PS loaded with NCs, indocyanine green (ICG) is attractive since it is an organic molecule and has an optical absorption peak at around 800 nm in the optical window of tissue. However, naked ICG is not useful due to its rapid excretion and clearance from the body and inefficient tumor affinity. Lactosome is a nanomicelle that is assembled from block copolymers, poly(sarcosine)–poly(L-lactic acid) (PS-PLLA) [5]. ICG-loaded lactosome (ICG-lactosome) is produced from synthesized PS-PLLA and ICG-labeled PLLA (ICG-PLLA) [6–8]. Due to its highly hydrophilic property, ICG-lactosome has a high escape ability from the reticuloendothelial system in the liver and spleen and is thus highly stable in the bloodstream [6]. In addition, PLLA as well as poly (sarcosine) has high biocompatibly and biodegradability, and it can therefore be easily degraded by hydrolases in the liver and spleen. Thus, ICG-lactosome would be a hopeful new-generation agent for PDT. Actually, some studies have shown the efficacy of PDT with ICG-lactosome in animal models [9–12]. It has also been shown by fluorescence imaging that ICG-lactosome selectively accumulates in a tumor. However, fluorescence imaging cannot provide depth-resolved profiling of the PS in tissue, and information on the pharmacokinetics of ICG-lactosome is therefore limited. Photoacoustic (PA) imaging, which is based on the detection of thermoelastic waves originating from chromophores in tissue, can be used for visualizing the depth distribution of a drug in

* Corresponding author.
E-mail address: ssato-bits@ndmc.ac.jp (S. Sato).

https://doi.org/10.1016/j.pdpdt.2019.04.031
Received 10 January 2019; Received in revised form 4 April 2019; Accepted 29 April 2019
Available online 01 May 2019

tissue [13–18]. PA imaging also enables visualization of blood vessels, including the neovasculature in a tumor, by light excitation with a wavelength near the hemoglobin peak [19–23]. Thus, PA imaging can be a powerful tool for monitoring vascular shutdown effects, which are important PDT mechanisms for tumor treatment [24,25].

The purpose of this study was to investigate the usefulness of PA imaging for monitoring both the pharmacokinetics and vascular damage in PDT with ICG-lactosome in a subcutaneous tumor mouse model. Since it is known that ICG solutions show concentration-dependent aggregation, which can affect their absorption characteristics and hence PA signal generation [26,27], we first measured the absorbance and PA spectra of two ICG-lactosome solutions with different ICG concentrations in micelles. Based on the results, we chose the solution suitable for *in vivo* experiments in which we performed PA imaging of the distributions of both ICG-lactosome and blood vessels in a subcutaneous tumor before and after PDT. We examined the accumulation and bleaching of PS as well as vascular responses in PDT with ICG-lactosome.

2. Materials and methods

2.1. Measurements of absorbance and PA spectra of ICG-lactosome solutions

We measured the absorbance and PA spectra of two ICG-lactosome solutions with a low ICG concentration (2 nmol/mg) and a high ICG concentration (27 nmol/mg) in micelles. The dose of 2 nmol/mg is the minimum ICG concentration in lactosome that was reported to show PDT efficacy *in vivo*, to our knowledge [9]. At the dose of 27 nmol/mg, on the other hand, the corresponding molar concentration of ICG-PLLA against PS–PLLA (˜20 mol%) is close to the maximum inclusion concentration without a diameter change of lactosome [28]. For both solutions, ICG-lactosome was dissolved in saline at an ICG molar concentration of 10 nmol/mL. The absorbance of each solutions was measured by a spectrophotometer (Hitachi High-Technologies Corporation, U-3300) in the wavelength range of 600–900 nm. PA spectroscopic measurements were conducted with a single-element, ring-shaped lead zirconate titanate (PZT) film ultrasound sensor (center frequency, 10 MHz). A quartz fiber (core diameter, 600 μm; NA, 0.39) was set at the center of the sensor; the fiber's output end face was in contact with the surface of each ICG-lactosome solution. Light pulses from a 100-Hz optical parametric oscillator (OPO; OPOTEK Opolette HR 355 LD; pulse width, 9 ns) were delivered through the fiber and PA signals originating from ICG-lactosome were detected with the sensor. The light wavelength was tuned in the range of 710–910 nm to obtain PA spectra of the ICG-lactosome solutions.

2.2. Animal model

Animal studies were approved by the Committee on Ethics of Animal Experiments in the National Defense Medical College (#12030). We used FaDu cells as a standard, stable cell line for an animal study on human head and neck squamous cell cancer. This cell line is also known to have low metastasis ability and is thus suitable for making a primary tumor model. FaDu cells were cultured in Dulbecco's Modified Eagle's Medium (Thermo Fisher Scientific) supplemented with 10% fetal bovine serum (HyClone Laboratories) and 1% pen-strep (Thermo Fisher Scientific). The cells were maintained in humidified air containing 5% CO_2 at 37°C. BALB/c nude mice (female, 7–9 weeks old) were anesthetized with isoflurane at a dose of 1% in pure oxygen at a flow rate of 1 L/min. To induce a solid tumor, 4×10^6 FaDu cells in 40 μl Hank's balanced salt solution (HBSS; Thermo Fisher Scientific) were subcutaneously injected into the left rear flank area of each mouse. Mice were used for experiments when the estimated tumor volume had reached ˜113 mm^3.

2.3. Setup for in vivo PA imaging

We used a home-made acoustic-resolution PA imaging system to visualize distributions of ICG-lactosome and blood vessels in the tumor. The system was described in detail previously [29,30]. Briefly, obliquely arranged quadruple optical fibers (core diameter, 600 μm; NA, 0.39) with incident angles at 45° were placed around a 50 MHz ultrasound sensor (Olympus V214-BB-RM) with an acoustic lens (radius of curvature, 5.7 mm), and the bottom of the sensor was immersed and scanned in water in a small container with a window in the bottom plate; the window was sealed with an optically and acoustically transparent polyethylene membrane (thickness, 30 μm). The axial and lateral resolutions of the sensor are 39 and 58 μm, respectively [31]. In this study, we used a 30-Hz optical parametric oscillator (OPO; Spectra-Physics M-OPO710; pulse width, 6 ns) or the above-described 100-Hz OPO for PA excitation. The former was used for PA imaging of the distribution of ICG-lactosome at 796 nm, which corresponds to the absorption peak of ICG-lactosome. The latter was tuned at 532 nm, which is close to one of the isosbestic points of oxy- and deoxy-hemoglobin, for PA imaging of blood vessels. Pulsed light energy for irradiation from each fiber was adjusted to 200 μJ at 796 nm or 170 μJ at 532 nm. The maximum light fluence on the tissue surface was 15.5 mJ/cm^2, which was lower than the American National Standards Institute (ANSI) safety limit (20 mJ/cm^2) [32]. The PA probe was automatically scanned over a 3.9 mm × 3.9 mm region of interest (ROI) with a step size of 50 μm for imaging of blood vessels or a step size of 150 μm for imaging of the distribution of ICG-lactosome. PA signals induced by 4 light pulses were averaged and recorded at each point of measurement. Raw temporal waveforms of the PA signals were converted into depth profiles by using a sound velocity of tissue (1540 m s^{-1}), based on which PA images were produced.

2.4. PA imaging for assessing ICG-lactosome and blood vessel distributions and PDT

Fig. 1 shows a time chart for the animal experiment in this study. First, PA imaging was performed to visualize the distribution of ICG-lactosome in the tumor with 796-nm light pulses at 30 min before and 30 min after injection of a saline solution of 1.5 wt% ICG-lactosome into the tail vein in each mouse (150 mg/kg animal weight). Hara et al.

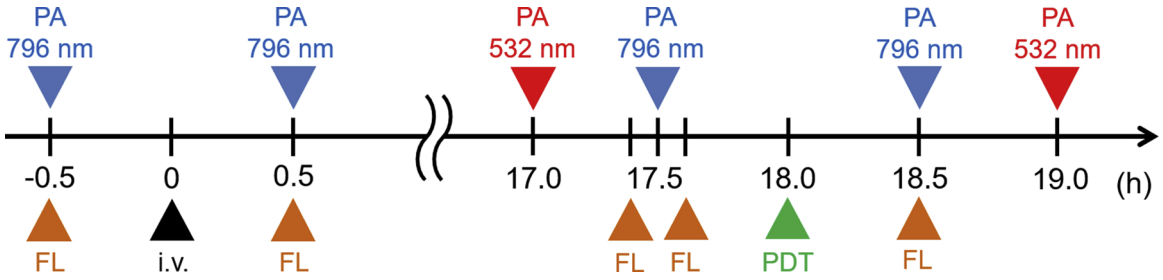

Fig. 1. Time chart of the experiment of PA and FL imaging and PDT for subcutaneous tumors in mice.

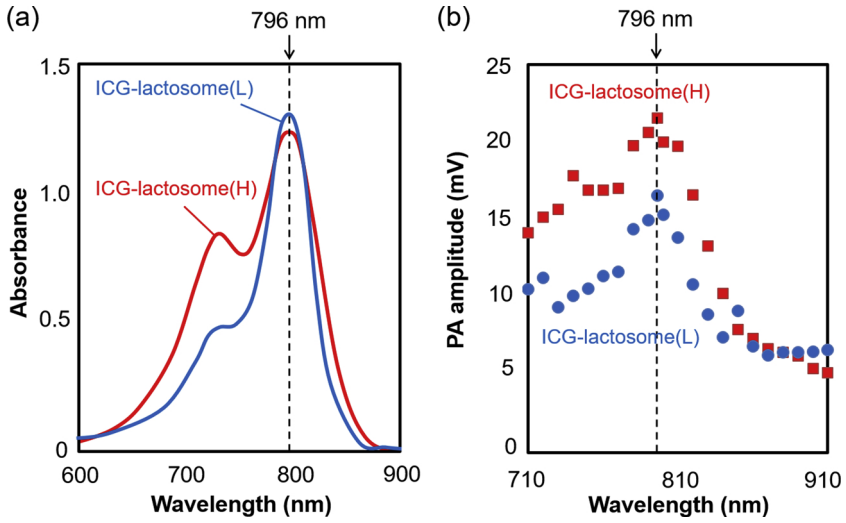

Fig. 2. (a) Absorption and (b) PA spectra of solutions of low-concentration ICG-lactosome (ICG-lactosome (L); 2 nmol/mg) and high-concentration ICG-lactosome (ICG-lactosome (H); 27 nmol/mg).

reported that even at an intravenous dose of 2000 mg/kg animal weight of lactosome in mice, their body weight did not significantly change when compared with control mice with saline injection until at least 11 days after the injection, indicating no toxicity [33]. The dose used in the present study was more than 10-times lower than the dose used in their study and thus can be said to be safe. We assessed the time course of fluorescence (FL) originating from ICG-lactosome distributed in the tumor and found that FL intensity was maximized at 18 h after injection and decreased slowly after that (data not shown). This indicates that PS was most efficiently accumulated at 18 h after injection and its clearance is inefficient. Thus, PDT was conducted at this time point by irradiation of the skin over the whole region of the tumor with a 10-mm spot size, CW laser from a fiber-coupled, 808-nm laser diode. The light intensity and duration were 600 mW/cm^2 and 10 min, respectively, the corresponding total light dose being 360 J/cm^2. PA imaging was performed with 532-nm light pulses at 1 h before and 1 h after PDT and with 796-nm light pulses at 30 min before and 30 min after PDT to examine the effects of PDT on the vasculatures and the photosensitizer in the tumor, respectively. Since the absorption spectra of ICG-lactosome and hemoglobin are only slightly overlapped, we can assume that PA imaging at 532 nm and that at 796 nm do not interfere with each other. During drug injection, PA imaging and PDT, mice were anesthetized with isoflurane at a dose of 1% in pure oxygen (flow rate, 1 L/min).

2.5. Fluorescence imaging of ICG-lactosome distribution

We used an ICG FL imaging system (Hamamatsu Photonics K.K., C10935-20; excitation wavelength, 760 nm; observation wavelength, 830 nm) to obtain FL images of ICG-lactosome distributions in the tumor. The FL images were compared with the MAP PA images at 796 nm. Since photobleaching of ICG-lactosome can be induced not only by the light for PDT but also by the light pulses for PA imaging, we also obtained FL images of ICG-lactosome in the tumor before and after PA imaging (796 nm) at 30 min prior to PDT to assess the latter effects (photobleaching by PA imaging). The time points for FL imaging are shown in Fig. 1.

2.6. Statistics

Statistical analysis was performed to compare amplitudes of PA signals originating from ICG-lactosome at each time point by the Friedman test with Scheffe's post hoc test. Amplitudes of PA signals originating from hemoglobin before and after PDT were compared by the Wilcoxon signed-rank test. In order to examine the correlation between the decreasing rate of PA amplitudes originating from ICG-lactosome and that from hemoglobin after PDT, a test of no correlation was performed. A value of $P < 0.05$ was regarded as statistically significant for all of the analyses.

3. Results and discussion

Fig. 2 shows (a) absorbances measured with a spectrophotometer and (b) PA spectra of the ICG-lactosome solutions with two ICG concentrations in micelles, 27 and 2 nmol/mg. All of the spectra measured by the two methods had peaks at 796 nm. The peak absorbance values measured with a spectrophotometer were similar for the two solutions, while the peak PA amplitude for the high ICG concentration solution was considerably higher than that for the low ICG concentration solution. This is attributable to the difference in Grüneisen parameters, which represent the thermoelastic efficiencies, of the two solutions. The results indicate that the ICG-lactosome with the high ICG concentration in micelles (27 nmol/mg) can more efficiently produce PA signals. Thus, we chose this type to be used for animal experiments.

Fig. 3(a) shows a white-light photograph of the skin over the tumor in a mouse before intravenous injection of ICG-lactosome. The red frame indicates the ROI for PA imaging (3.9 × 3.9 mm^2); all of the ROI was involved in the tumor, the outline of which is indicated by a black dotted line. Fig. 3(b–e) and (f, g) show maximum amplitude projection (MAP) PA images obtained at 796 nm (ICG-lactosome distribution) and 532 nm (blood vessels), respectively, and their corresponding PA tomograms (3.9 × 1.4 mm^2) at the scan lines shown by white broken lines: (b) before injection, (c) 30 min after injection, (d) 30 min before PDT, (e) 30 min after PDT, (f) 1 h before PDT and (g) 1 h after PDT. Yellow lines in the tomograms indicate the tissue surface. Before injection of ICG-lactosome, PA signal amplitudes at 796 nm were very low

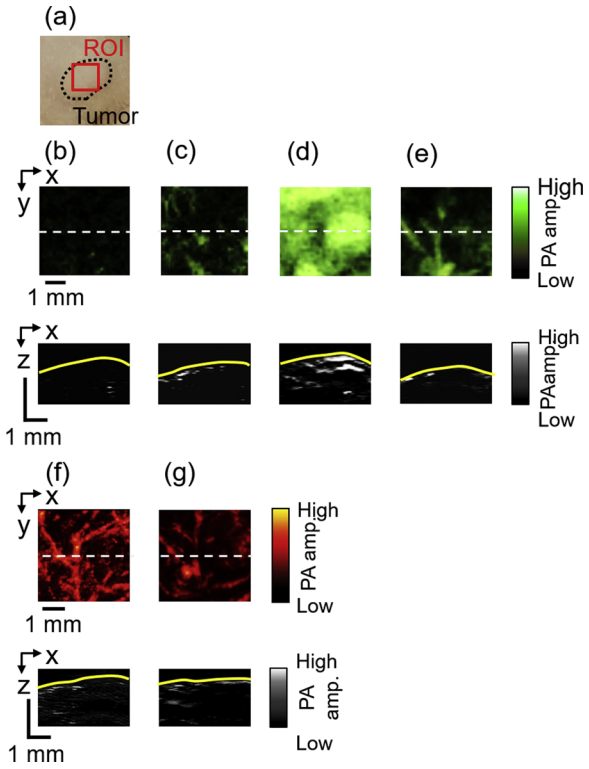

Fig. 3. (a) White-light photograph of the skin over the tumor in a mouse; the red frame indicates the ROI for PA imaging (3.9 × 3.9 mm^2). The black dotted line shows the outline of the tumor. (b–e) Maximum amplitude projection (MAP) PA images (3.9 × 3.9 mm^2) of the tumor at 796 nm and corresponding PA tomograms (3.9 × 1.4 mm^2) at the scan lines shown by white broken lines (distributions of ICG-lactosome): (b) before injection, (c) 30 min after injection, (d) 30 min before PDT and (e) 30 min after PDT. (f,g) MAP PA images (3.9 × 3.9 mm^2) of the tumor at 532 nm and corresponding tomograms (3.9 × 1.4 mm^2) at the scan lines shown by white broken lines (blood vessels) at 1 h before and 1 h after PDT, respectively. The yellow line in each tomogram indicates the tissue surface.

all over the ROI (Fig. 3b). At 30 min after injection, some PA signals originating from ICG-lactosome appeared in the subsurface region (Fig. 3c) and the distribution seemed to partially reflect the distribution of blood vessels (Fig. 3f), indicating that ICG-lactosome mainly existed in the vessels at this time point. However, since ICG-lactosome leaking out of the vessels was also visualized at 796 nm, the PA images at 796 nm were more blurred than those at 532 nm. At 30 min before PDT (at 17.5 h after injection), the PA signal amplitudes were increased remarkably (Fig. 3d) and the distribution was clearly different from that of blood vessels in both the horizontal and vertical directions (Fig. 3f), indicating efficient accumulation of ICG-lactosome in the tumor. The results of the ICG FL imaging showed that the PA imaging caused only a 0.78% decrease in the average FL intensity originating from ICG-lactosome in the tumor (n = 6) (data not shown), indicating a negligible photobleaching effect by the pulsed light excitation for PA imaging. At 30 min after PDT (18.5 h after injection), PA signal amplitudes originating from ICG-lactosome were decreased drastically, and there was some similarity between the distribution of ICG-lactosome (Fig. 3e) and that of blood vessels (Fig. 3g) after PDT, indicating efficient photobleaching in the extravascular space and hence in tumor cells. The change in the distribution of blood vessels after PDT (Fig. 3f,g) is discussed below.

Fig. 4(a) shows averaged maximum PA amplitudes originating from ICG-lactosome measured at all scanning points in the ROI at each time point (n = 8); the values are normalized by the values before injection. At 30 min before PDT, PA amplitude was significantly higher than that at 30 min after injection ($p < 0.05$), again indicating efficient accumulation of ICG-lactosome in the tumor. The amplitude was then decreased significantly by PDT; the value at 30 min after PDT was almost the same as that at 30 min after injection. This indicates considerable photobleaching of ICG-lactosome and hence the occurrence of an efficient photodynamic reaction in the tumor, since photobleaching of PS is known to be caused by singlet oxygen species produced through PDT reactions. Fig. 5(a–d) shows FL images of the ICG-lactosome distribution in the tumor (a) before injection, (b) 30 min after injection, (c) 30 min before PDT and (d) 30 min after PDT; red frames indicate ROIs for PA imaging. Fig. 5(e) shows average FL intensities in the ROI at each time point (n = 8). Its time course has a tendency similar to that of PA amplitude (Fig. 4a): both increased with the elapse of time before PDT and rapidly decreased after PDT. However, while there was a significant

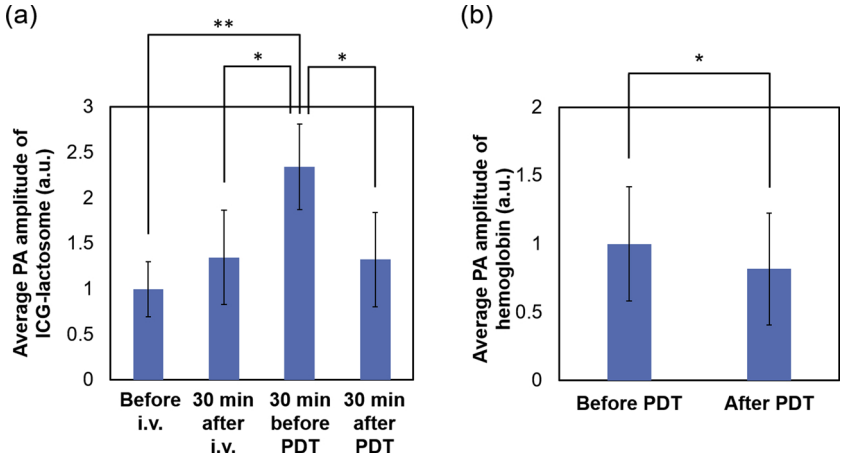

Fig. 4. Average PA amplitudes of (a) ICG-lactosome at each measurement time point (n = 8) and (b) hemoglobin before and after PDT (n = 6). Error bars represent standard deviation of the mean. Asterisks and double asterisks (*and**) depict $P < 0.05$ and $P < 0.01$, respectively.

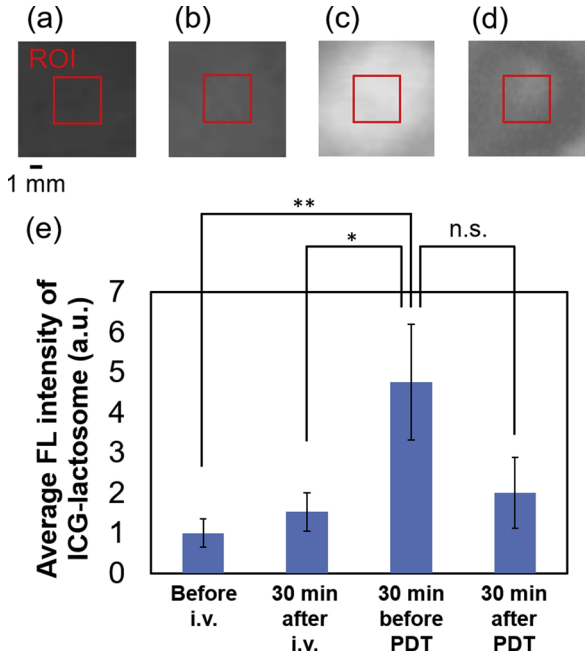

Fig. 5. (a–d) FL images of the skin over the tumor in a mouse: (a) before injection, (b) 30 min after injection, (c) 30 min before PDT and (d) 30 min after PDT. Red frames indicate ROIs for PA imaging (3.9 × 3.9 mm^2). (e) Average FL intensities of ICG-lactosome in the ROI at each time point (n = 8).

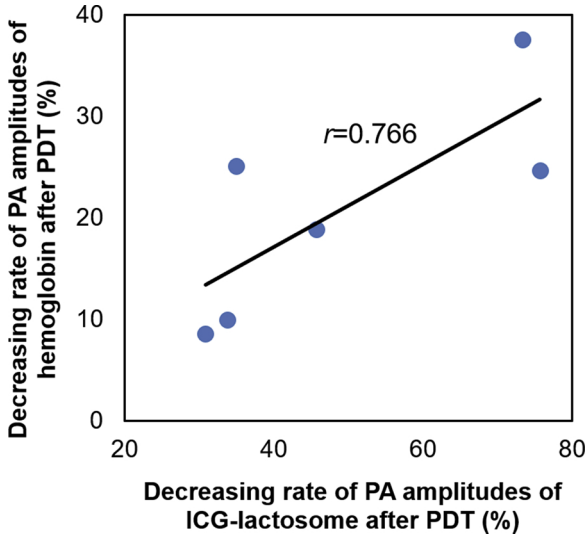

Fig. 6. Correlation between the decreasing rate of PA amplitudes of ICG-lactosome and the reduction rate of the PA amplitudes of hemoglobin due to PDT for the tumor.

difference between the PA amplitudes before and after PDT (Fig. 4a), there was no significant difference between the FL intensities at these two time points (Fig. 5e). This is attributable to the no depth-specific FL intensity signals.

PDT caused a drastic change in the PA signal distribution not only for ICG-lactosome but also for hemoglobin. Before PDT, the distribution of PA signal amplitudes of hemoglobin and hence blood vessels was observed in the tumor (Fig. 3f). As described above, the lateral resolution of the PA imaging sensor used was 58 μm [31], and blood vessels with diameters smaller than the lateral resolution, such as capillaries, could not be visualized clearly. After PDT, the signal level declined all over the ROI and PA signals originating from some parts of the blood vessels had disappeared (Fig. 3g). The corresponding tomograms also showed drastic decreases in PA signal amplitudes of hemoglobin in the whole depth region of interest. Fig. 4(b) shows averaged maximum PA amplitudes of hemoglobin at all scanning points in the ROI before and after PDT (n = 6); the values are normalized by the values before PDT. PA signal amplitudes of hemoglobin were significantly decreased after PDT, indicating vascular shutdown effects due to PDT. As the mechanism of PDT with ICG-lactosome, Tsujimoto et al. showed apoptosis induced in tumor cells by a terminal deoxynucleotidyl transferase-mediated dUTP nick-end labeling (TUNEL) method [11]. Tsuda et al. suggested that both the singlet oxygen and the heat generated by a photothermal reaction were involved in the antitumor effects in PDT with ICG-lactosome [12]. Our observation of a significant decrease in the PA signals of hemoglobin, *i.e.*, vascular shutdown effects, would be another mechanism in PDT with ICG-lactosome.

Fig. 6 shows the correlation between the decreasing rate of PA amplitudes of ICG-lactosome and that of hemoglobin after PDT. The correlation coefficient (r) was estimated to be 0.766, but the p value was 0.076, indicating that there is no significant correlation between the two variables. Although both the photobleaching of ICG-lactosome and the vascular shutdown can be caused by singlet oxygen species, their interactions with tumor cells and blood vessels and the outcomes should be affected by many factors such as microscopic PS distributions and blood vessel charcteristics. The nonsignificant correlation between the two events may reflect such complex environments involved in PDT reactions; for their analyses, PA imaging can play an important role.

In conclusion, we demonstrated the usefulness of dual-wavelength PA imaging that enables depth-resolved monitoring of accumulation and photobleaching of a PS in conjunction with vascular damage due to PDT. This method can be applied to PDTs with a wide variety types of PSs [15–18]. The observation depth of the PA imaging system used in this study is limited to a few millimeters, which is too shallow for clinical application. However, imaging depth can be increased to a few centimeters by sacrificing spatial resolution [34]; high-resolution imaging is not necessarily needed to monitor the distributions of a PS and blood vessels in tumors. The method can also be a powerful tool to investigate or develop next-generation PDTs.

Conflict of interest

The authors declare no conflict of interest.

Acknowledgments

This paper was partially prepared on the basis of data from chapter 3 in the PhD thesis of Y. Tsunoi [35]. The authors acknowledge Dr. Yoshihiro Miyagawa, Mr. Ryota Watanabe, Mr. Yusuke Akutsu and Ms. Tsuyako Ohkura for their technical assistance in the experiments. We also thank Advantest Corporation for the use of the optical parametric oscillator and the single element ultrasound sensor and the Department of Plastic and Reconstructive Surgery of National Defense Medical College for the use of the ICG FL imaging system. This work was partially supported by a grant from the Tateishi Science and Technology Foundation.

References

[1] Y. Matsumura, H. Maeda, A new concept for macromolecular therapeutics in cancer chemotherapy: mechanism of tumoritropic accumulation of proteins and the antitumor agent smancs, Cancer Res. 46 (12) (1986) 6387–6392.
[2] A. Mastera, M. Livingstona, A.S. Gupta, Photodynamic nanomedicine in the treatment of solid tumors: perspectives and challenges, J. Control. Release 168 (1) (2013) 88–102, https://doi.org/10.1016/j.jconrel.2013.02.020.
[3] M.E. Sherien, M.G. Amira, A.M.A. Mona, H.B. Ibrahim, A.W. Hanaa, B.A. Abdel-Rahman, Photodynamic therapeutic activity of indocyanine green entrapped in polymeric nanoparticles, Photodiag. Photodyn. Ther. 10 (2) (2013) 173–185, https://doi.org/10.1016/j.pdpdt.2012.08.003.
[4] O.J. Fakayode, N. Tsolekile, S.P. Songca, O.S. Oluwafemi, Applications of

functionalized nanomaterials in photodynamic therapy, Biophys. Rev. 10 (1) (2018) 49–67, https://doi.org/10.1007/s12551-017-0383-2.
[5] A. Makino, R. Yamahara, E. Ozeki, S. Kimura, Preparation of novel polymer assemblies, Chem. Lett. 36 (10) (2007) 1220–1221, https://doi.org/10.1246/cl.2007.1220.
[6] A. Makino, S. Kizaka-Kondoh, R. Yamahara, I. Hara, T. Kanzaki, E. Ozeki, M. Hiraoka, S. Kimura, Near-infrared fluorescence tumor imaging using nanocarrier composed of poly(l-lactic acid)-block-poly(sarcosine) amphiphilic polydepsipeptide, Biomaterials 30 (28) (2009) 5156–5160, https://doi.org/10.1016/j.biomaterials.2009.05.046.
[7] A. Makino, S. Kimura, Preparation of peptide- and protein-based molecular assemblies and their utilizations as nanocarriers for tumor imaging, React. Funct. Polym. 71 (3) (2011) 272–279, https://doi.org/10.1016/j.reactfunctpolym.2010.09.010.
[8] T. Funayama, M. Sakane, T. Abe, I. Hara, E. Ozeki, N. Ochiai, Intraoperative near-infrared fluorescence imaging with novel indocyanine green-loaded nanocarrier for spinal metastasis: a preliminary animal study, Open Biomed. Eng. J. 6 (2012) 80–84, https://doi.org/10.2174/1874120701206010080.
[9] T. Funayama, T. Tsukanishi, I. Hara, E. Ozeki, M. Sakane, Tumor-selective near-infrared photodynamic therapy with novel indocyanine green-loaded nanocarrier delays paralysis in rats with spinal metastasis, Photodiagnosis Photodyn. Ther. 10 (4) (2013) 374–378, https://doi.org/10.1016/j.pdpdt.2013.03.002.
[10] H. Tsujimoto, Y. Morimoto, R. Takahata, S. Nomura, K. Yoshida, H. Horiguchi, S. Hiraki, S. Ono, H. Miyazaki, D. Saito, I. Hara, E. Ozeki, J. Yamamoto, K. Hase, Photodynamic therapy using nanoparticle loaded with indocyanine green for experimental peritoneal dissemination of gastric cancer, Cancer Sci. 105 (12) (2014) 1626–1630, https://doi.org/10.1111/cas.12553.
[11] H. Tsujimoto, Y. Morimoto, R. Takahata, S. Nomura, K. Yoshida, S. Hiraki, H. Horiguchi, H. Miyazaki, S. Ono, D. Saito, I. Hara, E. Ozeki, J. Yamamoto, K. Hase, Theranostic photosensitive nanoparticles for lymph node metastasis of gastric cancer, Ann. Surg. Oncol. 22 (2015) 923–928, https://doi.org/10.1245/s10434-015-4594-0.
[12] T. Tsuda, M. Kaibori, H. Hishikawa, R. Nakatake, T. Okumura, E. Ozeki, I. Hara, Y. Morimoto, K. Yoshii, M. Kon, Near-infrared fluorescence imaging and photodynamic therapy with indocyanine green lactosome has antineoplastic effects for hepatocellular carcinoma, PLoS One 12 (8) (2017) e0183527, , https://doi.org/10.1371/journal.pone.0183527.
[13] D. Razansky, C. Vinegoni, V. Ntziachristos, Multispectral photoacoustic imaging of fluorochromes in small animals, Opt. Lett. 32 (19) (2007) 2891–2893, https://doi.org/10.1364/OL.32.002891.
[14] Y. Tsunoi, S. Sato, S. Kawauchi, H. Ashida, D. Saitoh, M. Terakawa, *In vivo* photoacoustic molecular imaging of the distribution of serum albumin in rat burned skin, Burns 39 (7) (2013) 1403–1408, https://doi.org/10.1016/j.burns.2013.03.007.
[15] C.J. Ho, G. Balasundaram, W. Driessen, R. McLaren, C.L. Wong, U.S. Dinish, A.B. Attia, V. Ntziachristos, M. Olivo, Multifunctional photosensitizer-based contrast agents for photoacoustic imaging, Sci. Rep. 4 (2014) 5342, https://doi.org/10.1038/srep05342.
[16] A.B. Attia, G. Balasundaram, W. Driessen, V. Ntziachristos, M. Olivo, Phthalocyanine photosensitizers as contrast agents for *in vivo* photoacoustic tumor imaging, Biomed. Opt. Express 6 (2) (2015) 591–598, https://doi.org/10.1364/BOE.6.000591.
[17] A. Hirao, S. Sato, D. Saitoh, N. Shinomiya, H. Ashida, M. Obara, *In vivo* photoacoustic monitoring of photosensitizer distribution in burned skin for antibacterial photodynamic therapy, Photochem. Photobiol. 86 (2) (2010) 426–430, https://doi.org/10.1111/j.1751-1097.2009.00683.x.
[18] Y. Tsunoi, S. Sato, H. Ashida, M. Terakawa, Photoacoustic imaging of intravenously injected photosensitizer in rat burn models for efficient antibacterial photodynamic therapy, Proc. SPIE 8210 (2012) 82100D, , https://doi.org/10.1117/12.907644.
[19] K. Maslov, G. Stoica, L.V. Wang, *In vivo* dark-field reflection-mode photoacoustic microscopy, Opt. Lett. 30 (6) (2005) 625–627, https://doi.org/10.1364/OL.30.000625.
[20] Y. Tsunoi, S. Sato, R. Watanabe, S. Kawauchi, H. Ashida, M. Terakawa, Compact acoustic-resolution photoacoustic imaging system with fiber-based illumination, Jpn. J. Appl. Phys. 53 (12) (2014) 126701, , https://doi.org/10.7567/JJAP.53.126701.
[21] M. Omar, D. Soliman, J. Gateau, V. Ntziachristos, Ultrawideband reflection-mode optoacoustic mesoscopy, Opt. Lett. 39 (13) (2014) 3911–3914, https://doi.org/10.1364/OL.39.003911.
[22] M. Omar, M. Schwarz, D. Soliman, P. Symvoulidis, V. Ntziachristos, Pushing the optical imaging limits of cancer with multi-frequency-band Raster-Scan Optoacoustic Mesoscopy (RSOM), Neoplasia 17 (2) (2015) 208–214, https://doi.org/10.1016/j.neo.2014.12.010.
[23] J. Laufer, P. Johnson, E. Zhang, B. Treeby, B. Cox, B. Pedley, P. Bearda, *In vivo* preclinical photoacoustic imaging of tumor vasculature development and therapy, J. Biomed. Opt. 17 (5) (2012) 056016, , https://doi.org/10.1117/1.JBO.17.5.056016.
[24] L. Xiang, D. Xing, H. Gu, D. Yang, S. Yang, L. Zeng, W.R. Chen, Real-time optoacoustic monitoring of vascular damage during photodynamic therapy treatment of tumor, J. Biomed. Opt. 12 (1) (2007) 014001, , https://doi.org/10.1117/1.2437752.
[25] P. Shao, D.W. Chapman, R.B. Moore, R.J. Zemp, Monitoring photodynamic therapy with photoacoustic microscopy, J. Biomed. Opt. 20 (10) (2015) 106012, , https://doi.org/10.1117/1.JBO.20.10.106012.
[26] M.L. Landsman, G. Kwant, G.A. Mook, W.G. Zijlstra, Light-absorbing properties, stability, and spectral stabilization of indocyanine green, J. Appl. Physiol. 40 (4) (1976) 575–583.
[27] G. Kim, S.W. Huang, K.C. Day, M. O'Donnell, R.R. Agayan, M.A. Day, R. Kopelman, S. Ashkenazi, Indocyanine-green-embedded PEBBLEs as a contrast agent for photoacoustic imaging, J. Biomed. Opt. 12 (4) (2007) 044020, , https://doi.org/10.1117/1.2771530.
[28] A. Makino, E. Hara, I. Hara, R. Yamahara, K. Kurihara, E. Ozeki, F. Yamamoto, S. Kimura, Control of *in vivo* blood clearance time of polymeric micelle by stereochemistry of amphiphilic polydepsipeptides, J. Control. Release 161 (3) (2012) 821–825, https://doi.org/10.1016/j.jconrel.2012.05.006.
[29] Y. Tsunoi, K. Yoshimi, R. Watanabe, N. Kumai, M. Terakawa, S. Sato, Theranostic system for drug delivery and pharmacokinetic imaging based on nanosecond pulsed light-induced photomechanical and photoacoustic effects, Jpn. J. Appl. Phys. 54 (11) (2015) 116601, , https://doi.org/10.7567/JJAP.54.116601.
[30] Y. Tsunoi, S. Sato, S. Kawauchi, Y. Akutsu, Y. Miyagawa, K. Araki, A. Shiotani, M. Terakawa, Quality improvement of acoustic-resolution photoacoustic imaging of skin vasculature based on practical synthetic-aperture focusing and bandpass filtering, Jpn. J. Appl. Phys. 57 (12) (2018) 127001, , https://doi.org/10.7567/JJAP.57.127001.
[31] R. Watanabe, S. Sato, Y. Tsunoi, S. Kawauchi, T. Takemura, M. Terakawa, Photoacoustic imaging for transvascular drug delivery to the rat brain, Proc. SPIE 9305 (2015) 930523, , https://doi.org/10.1117/12.2078505.
[32] American National Standards Institute, American National Standard for Safe Use of Lasers: ANSI Z136. 1-2007, Laser Institute of America, Orlando, 2007.
[33] E. Hara, A. Makino, K. Kurihara, M. Sugai, A. Shimizu, I. Hara, E. Ozeki, S. Kimura, Evasion from accelerated blood clearance of nanocarrier named as "Lactosome" induced by excessive administration of Lactosome, Biochim. Biophys. Acta 1830 (8) (2013) 4046–4052, https://doi.org/10.1016/j.bbagen.2013.03.024.
[34] L.V. Wang, S. Hu, Photoacoustic tomography: in vivo imaging from organelles to organs, Science 335 (6075) (2012) 1458–1462, https://doi.org/10.1126/science.1216210.
[35] Y. Tsunoi, Integrated system for drug delivery and pharmacokinetic imaging based on nanosecond pulsed light-induced photomechanical and photoacoustic effect, Doctoral Thesis, Keio University, Yokohama, 2016.